

# Octahedral tilt-driven phase transitions in $\text{BaZrS}_3$ chalcogenide perovskite

Prakriti Kayastha,<sup>†</sup> Erik Fransson,<sup>‡</sup> Paul Erhart,<sup>‡</sup> and Lucy Whalley<sup>\*,†</sup>

<sup>†</sup>*Department of Mathematics, Physics and Electrical Engineering, Northumbria University, Newcastle upon Tyne, NE1 8QH, United Kingdom*

<sup>‡</sup>*Department of Physics, Chalmers University of Technology, SE-41296, Gothenburg, Sweden*

E-mail: l.whalley@northumbria.ac.uk

## Abstract

Chalcogenide perovskites are lead-free materials for potential photovoltaic or thermoelectric applications.  $\text{BaZrS}_3$  is the most studied member of this family due to its superior thermal and chemical stability, desirable optoelectronic properties, and low thermal conductivity. Phase transitions of the  $\text{BaZrS}_3$  perovskite are under-explored in literature as most experimental characterization is performed at ambient conditions where the orthorhombic  $Pnma$  phase is reported to be stable. In this work, we study the dynamics of  $\text{BaZrS}_3$  across a range of temperatures and pressures using an accurate machine-learned interatomic potential trained with data from hybrid density functional theory calculations. At 0 Pa, we find a first-order phase transition from the orthorhombic to tetragonal  $I4/mcm$  phase at 610 K, and a second-order transition from the tetragonal to the cubic  $Pm\bar{3}m$  phase at 880 K. The tetragonal phase is stable over a larger temperature range at higher pressures. To confirm the validity of our model we report the static structure factor as a function of temperature and compare our results with published experimental data.

## 1 Introduction

Chalcogenide perovskites have gained relevance as lead-free photovoltaic absorber materials<sup>1-5</sup>

as they exhibit strong light absorption<sup>6</sup> and dielectric screening<sup>7</sup> alongside desirable defect properties.<sup>8,9</sup>  $\text{BaZrS}_3$  is the most studied member of this family with research efforts including material synthesis at moderate temperatures,<sup>10-14</sup> band-gap engineering,<sup>15-17</sup> and a proof-of-concept solar cell.<sup>18</sup>  $\text{BaZrS}_3$  has also been explored as a potential thermoelectric material as it displays fast electronic transport<sup>19</sup> coupled with low thermal conductivity,<sup>20</sup> leading to record-high  $zT$  values among reported halide and chalcogenide perovskite materials.<sup>21</sup>

Whilst  $\text{BaZrS}_3$  is reported to retain stability in a perovskite structure above 1000 K,<sup>22</sup> the vast majority of materials characterization is carried out at ambient conditions.<sup>10,11,23,24</sup> At room temperature, the consensus is that  $\text{BaZrS}_3$  is stable in an orthorhombic  $Pnma$  perovskite structure, as confirmed by both experimental<sup>13,25,26</sup> and computational studies.<sup>20,27-29</sup> Above this temperature, the picture is less clear. Recent temperature-dependent X-ray diffraction (XRD) measurements show a discontinuous change in the lattice parameters at 780 K, indicating a first-order phase transition.<sup>22,30</sup> However, Raman spectroscopy does not confirm this finding,<sup>31</sup> likely due to the structural and dynamic similarity of perovskite phases coupled with significant thermal broadening.

Many  $\text{ABX}_3$  perovskites undergo tilt-driven phase transitions to form lower-symmetry poly-

morphs with antiferrodistortive displacement patterns.<sup>32</sup> The prototypical high-temperature perovskite phase is a cubic structure. As the temperature is reduced, lower-symmetry tetragonal and orthorhombic perovskite phases can be formed through tilting of the  $BX_6$  octahedra.<sup>33,34</sup> Therefore, it is likely that there are transitions to higher symmetry phases at temperatures above ambient for  $BaZrS_3$ . An understanding of the exact  $BaZrS_3$  perovskite structure is important as a phase transition within the operational temperature range of solar cells ( $-20^\circ\text{C}$  to  $60^\circ\text{C}$ ) or thermoelectric generators ( $100^\circ\text{C}$  to  $800^\circ\text{C}$ ) might impact key functional properties.<sup>35</sup> Anharmonic dynamics are also crucial for quantitative predictions of electron-phonon coupling and related optical properties.

In this work, we use molecular dynamics (MD) to sample the anharmonic free energy surface and simulate the finite-temperature dynamics of the  $BaZrS_3$  perovskite. We accelerate the calculation of energies, forces, and stresses necessary for MD by constructing a machine learning potential using reference data from density functional theory (DFT) calculations using a hybrid exchange-correlation functional. We use known group-subgroup relationships to systematically identify which octahedral tilt patterns can be accessed during phase transitions. We identify two phase transitions in  $BaZrS_3$  at 0 Pa: a first-order orthorhombic  $Pnma$  to tetragonal  $I4/mcm$  transition at 610 K and a second-order tetragonal to cubic  $Pm\bar{3}m$  phase transition at 880 K. We construct a phase diagram for  $BaZrS_3$  across a pressure and temperature range of  $-4$  GPa to 10 GPa and 0 K to 1200 K, respectively. Lastly, we predict temperature-dependant static structure factors for comparison against XRD measurements, and compare our predictions against published experimental data.

## 2 Methods

A machine learning potential was constructed using the neuroevolution potential (NEP) method implemented in the GPUMD pack-

age.<sup>36</sup> The ASE<sup>37</sup> and CALORINE<sup>38</sup> packages were used to prepare the training structures, set up MD simulations, and post-process the results. The training set consisted of 1187 structures. This included cubic, tetragonal, and orthorhombic perovskite structures with applied strain or small random displacements, all 15 Glazer-tilt structures,<sup>39,40</sup> and snapshots from NPT MD simulations. DFT calculations were performed using the FHI-aims code<sup>41</sup> and the HSE06 exchange-correlation functional.<sup>42</sup> The root mean squared training errors were 1.8 meV/atom, 72.2 meV/Å, and 28.9 meV/atom for formation energies, forces, and virials, respectively (see Fig. S2 for the corresponding parity plots). Symmetry-constrained geometry relaxations as implemented in ASE<sup>37</sup> were performed until the maximal force component was below  $10^{-3}$  eV/Å. Harmonic phonon dispersions were evaluated using the PHONOPY package<sup>43</sup> with a  $2 \times 2 \times 2$  supercell and a 0.01 Å displacement.

Heating and cooling simulations with supercells of 40960 atoms were run in the NPT ensemble in the temperature range of 0 K to 1200 K and a pressure range of  $-4$  GPa to 10 GPa using a timestep of 1 fs. To identify the symmetry group formed, atomic displacements were projected onto the octahedral-tilt phonon eigenvectors of the cubic structure, as outlined in Ref. 44. Free energy calculations were carried out using thermodynamic integration (TI) with an Einstein crystal as reference Hamiltonian.<sup>45</sup> To calculate the static structure factor  $S(\mathbf{q})$  the DYNASOR package<sup>46</sup> was used to post-process NVT MD simulations. For more computational details see the Supplementary Information.

## 3 Results and discussion

The aristotype cubic  $Pm\bar{3}m$  phase is the simplest perovskite form. However, perovskites often adopt lower-symmetry, distorted non-cubic phases.<sup>47</sup> Distortions in the cubic perovskite give rise to a wide range of structures which can be classified into three categories.<sup>48,49</sup> (i)  $BX_6$  octahedral tilting; (ii) distortions of the

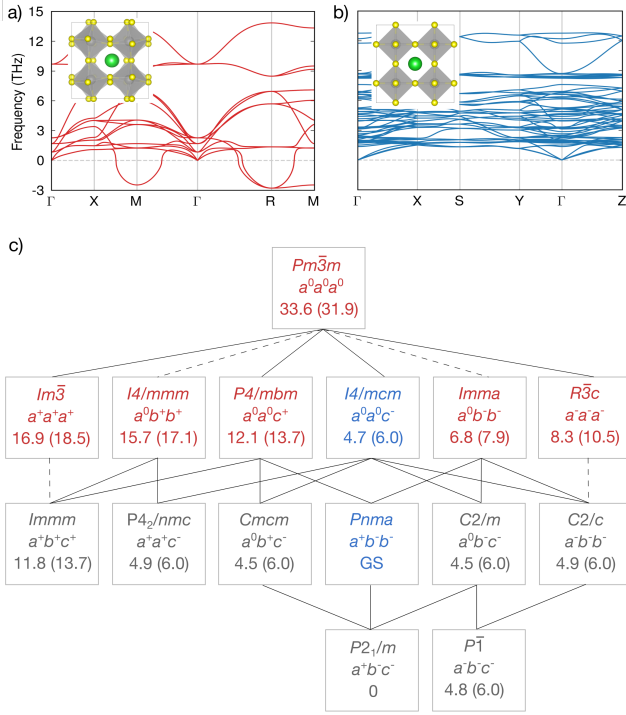


Figure 1: DFT-calculated crystal and phonon band structures of the (a) orthorhombic  $Pnma$  (b) and cubic  $Pm\bar{3}m$  phases. Green, grey, and yellow spheres represent Ba, Zr, and S atoms respectively. (c) Group-subgroup relationships and formation energies. The space group, Glazer notation, and formation energy are specified for each phase accessible through octahedral tilting. The formation energies (in meV/atom) with respect to the ground state (GS)  $Pnma$  phase obtained from DFT and NEP model calculations (in parentheses) are reported in the bottom rows. Connecting lines indicate group-subgroup relationships. Dashed lines indicate transitions that must be first order according to Landau theory.<sup>40</sup> Red text denotes the presence of imaginary phonon modes (dynamic instability). Blue text denotes dynamic stability. Grey text denotes that the phase is symmetrically equivalent to a supergroup structure after relaxation; there is still a small discrepancy in formation energy, which is discussed in the Supplementary Information. Adapted from Howard and Stokes.<sup>40</sup>

$BX_6$  octahedra; and (iii) B-site cation displacements. Octahedral tilting leads to 15 possible space groups as identified by Glazer.<sup>39</sup>

In Fig. 1a and b, we plot the harmonic phonon dispersions and crystal structures of the cubic  $Pm\bar{3}m$  and the experimentally observed  $Pnma$  phase. The cubic  $Pm\bar{3}m$   $BaZrS_3$  phase ( $a^0a^0a^0$  in Glazer notation) is dynamically unstable indicating the presence of a lower-symmetry stable structure at 0 K.<sup>50</sup> The imaginary phonon modes at the M point of the Brillouin zone correspond to in-phase (+) tilting of the  $ZrS_6$  octahedra and are described with the irrep  $M_2^+$  (for a unit cell with an origin at the Ba-site). The imaginary modes at the R point correspond to out-of-phase (-) tilting and have irrep  $R_5^-$ . Both modes are triply degenerate. Distortions along one M-mode and two perpendicular R-modes result in a dynamically stable orthorhombic  $Pnma$  phase ( $a^-a^-c^+$ ). The dynamic and energetic stability of the orthorhombic phase at 0 K is in agreement with previous experimental and DFT studies reporting it to be stable at low temperatures.<sup>51-53</sup>

Distortions along linear combinations of the M- and R-modes result in 15 unique space groups. We display the group-subgroup relationships and 0 K formation energies for  $BaZrS_3$  in Fig. 1c. As expected,  $Pm\bar{3}m$  is the highest energy phase relative to the  $Pnma$  ground state.  $I4/mcm$  is 4.7 meV/atom above the ground state, indicating that it may form as a higher temperature phase. The comprehensive mapping across all possible structures ensures that we include all phases that might be formed at high temperatures in our training data for the NEP machine learning potential.

Connecting lines in Fig. 1c indicate group-subgroup relationships between structures. In Landau theory, this relationship is necessary (but not sufficient) for structures connected through second-order (continuous) phase transitions.<sup>54</sup> Dashed lines indicate that, despite sharing a group-subgroup relationship, the phase transition must be first-order (discontinuous) in Landau theory.<sup>55</sup>

In Fig. 2, we plot properties observed and derived from MD simulations spanning 0 K to 1200 K and 200 ns. When heating the low-

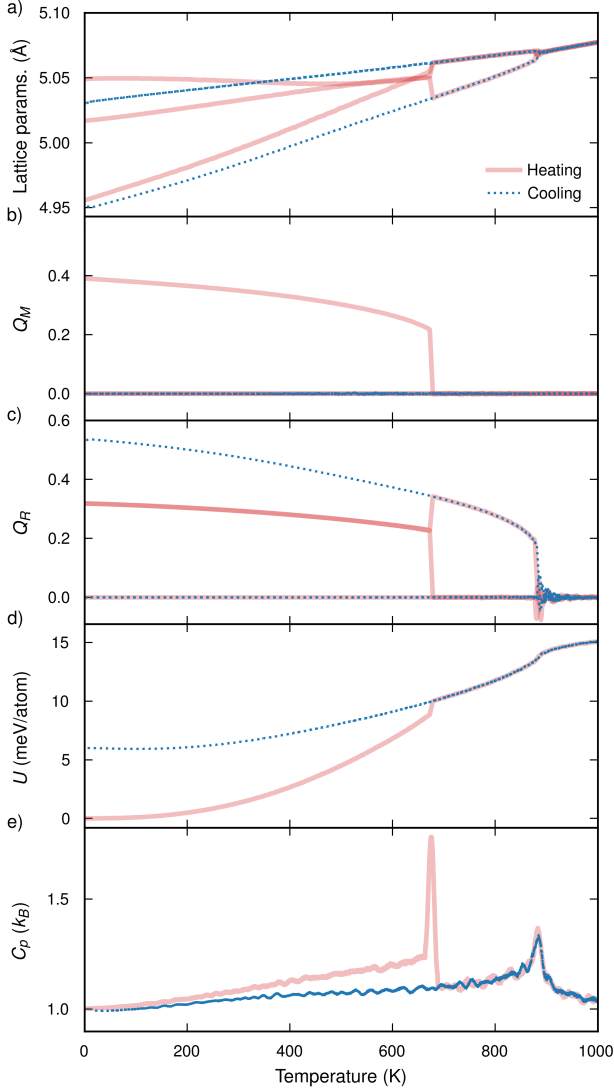


Figure 2: Properties of the BaZrS<sub>3</sub> perovskite from cooling (blue) and heating (red) simulations: (a) pseudo-cubic lattice parameters; (b) M-mode and (c) R-mode amplitudes ( $Q_M$ ,  $Q_R$ ); (d) energies ( $U$ ); (e) heat capacities ( $C_p$ ). Energies are shown relative to the  $Pnma$  ground state energy at 0 K. The heat capacity is obtained by calculating the numerical derivative of the energy with respect to temperature,  $C_p = dU/dT$ . All quantities are averaged over a time period corresponding to 5 K. The data suggests a first-order phase transition at 650 K and a second-order phase transition at 900 K.

temperature  $Pnma$  structure there are phase transitions at 650 K and 880 K. The transition at 650 K is accompanied by a discontinuous and sharp change in lattice parameters (Fig. 2a). Two of the lattice parameters become equal, indicating an orthorhombic to tetragonal transition. In contrast, the transition at 880 K is gradual and continuous. All three lattice parameters become equal, indicating a tetragonal-to-cubic transition.

In Fig. 2b,c we show projections of the M and R phonon modes on structures sampled from the simulation. From 0 K to 650 K, two R-modes and one M-mode are active, corresponding to the  $Pnma$  phase ( $a^-a^-c^+$ ). This confirms the existence of the  $Pnma$  structure at room temperature as reported in several experimental studies.<sup>27,56</sup> From 650 K to 880 K, only one R-mode is activated corresponding to the tetragonal  $I4/mcm$  phase ( $a^0a^0c^-$ ). Above 900 K, no modes are activated indicating the existence of a cubic  $Pm\bar{3}m$  phase ( $a^0a^0a^0$ ).

A sharp discontinuity is observed in energy (Fig. 2d) and heat capacity (Fig. 2e) at 650 K. The 1 meV/atom energy change is the latent heat associated with a first-order phase transition and is comparable to that observed in other perovskites.<sup>33,34</sup> At 880 K a continuous change in energy is observed, typical of second-order phase transitions, resulting in a broader, less pronounced peak in the heat capacity. We conclude that there is a first-order  $Pnma$ -to- $I4/mcm$  transition at 650 K, and a second-order  $I4/mcm$ -to- $Pm\bar{3}m$  transition at 880 K. These observations are consistent with the group-subgroup analysis presented in Fig. 1. The  $Pnma$  phase does not share a group-subgroup relationship with  $I4/mcm$ , necessitating a first-order phase transition. In contrast,  $I4/mcm$  is a subgroup of the  $Pm\bar{3}m$  phase, so can be accessed through a second-order transition.

In the cooling runs, we start from the high-temperature  $Pm\bar{3}m$  structure and reproduce the heating behavior for the second-order transition at 880 K. Significant hysteresis is observed for the first-order phase transition at 650 K as the system cannot overcome the free energy barrier required to form the orthorhom-

bic phase. Due to the stochastic nature of MD simulations, we do recover the orthorhombic phase in some of the cooling runs (see Supplementary Information).

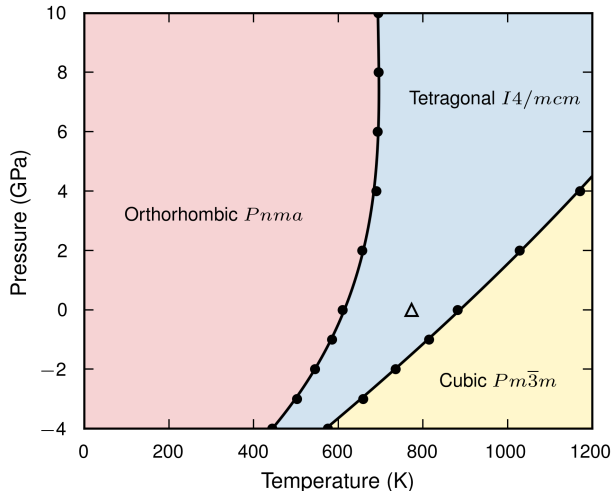


Figure 3: Phase diagram of  $\text{BaZrS}_3$  as a function of pressure and temperature. The triangle corresponds to the experimental orthorhombic-to-tetragonal phase transition temperature reported in Ref. 30.

In many perovskite materials transitions to new phases can be induced through pressure. Strain engineering in a device stack can be realised through coherent interface formation with a suitably matched substrate.<sup>57</sup> In Fig. 3, we present the  $\text{BaZrS}_3$  pressure-temperature phase diagram across  $-4$  GPa to 10 GPa and 0 K to 1000 K. To accurately predict the first-order  $Pnma$ -to- $I4/mcm$  phase transition temperatures we use thermodynamic integration to calculate free energies. This avoids the numerical limitations of a kinetic approach which must overcome the first-order transition barrier.<sup>34</sup> The second-order  $I4/mcm$ -to- $Pm\bar{3}m$  phase transition temperatures are calculated from heating runs in the NPT ensemble.

The higher symmetry phases are stabilised with increasing temperature or decreasing pressure. This indicates that the  $\text{ZrS}_6$  octahedra are relatively rigid, with volume expansion driven through decreased octahedral tilting;<sup>58</sup> see Sect. for further discussion. At ambient pressure the  $Pnma$ -to- $I4/mcm$  phase transition temperature is 610 K. Above 4 GPa, the

transition temperature saturates at 690 K.

Transitions between structurally similar perovskite phases are not always discernible in Raman spectra, as the peak splitting can be less than the peak broadening resulting from thermal fluctuations or higher-order scattering.<sup>59–61</sup> Raman measurements at ambient temperature show that the  $Pnma$  phase is stable between 0 GPa to 8.9 GPa,<sup>27</sup> in agreement with our results. Raman measurements between 10 K to 875 K show no indication of a first-order phase transition at  $\sim 650$  K,<sup>31</sup> however, the lowest frequency Raman peak shows a marked red shift with increasing temperature up to 875 K, which could be a signature of the second-order soft mode transition we predict at 880 K.

Temperature-dependent XRD data shows a reversible first-order orthorhombic-to-tetragonal phase transition at elevated temperatures,<sup>22,30</sup> in agreement with our results. The measurements are partially obstructed by the degradation of  $\text{BaZrS}_3$  through oxidation, which occurs in the same temperature range as the phase transition. This might contribute towards the quantitative discrepancy between the experimentally measured transition at 773 K,<sup>30</sup> and our predicted transition at 610 K. Above this phase transition temperature, the two unique lattice parameters converge,<sup>22</sup> which we also observe whilst approaching the second-order transition in our MD simulation (Fig. 2a).

We present the temperature-dependent static structure factors at ambient pressure in Fig. 4. At high temperature, the characteristic peaks of a cubic perovskite are clearly identified (Fig. 4a). Below 900 K, R-mode activation produces a doubling of the unit-cell along one axis and the appearance of superlattice peaks at half-integer planes (Fig. 4b). Peak splittings of the cubic diffraction lines are also observed. The splittings indicate a tetragonal distortion, with the largest splitting corresponding to a  $h00$  reflection (200), and the  $hhh$  reflection (111) remaining a singlet.<sup>49</sup> Experimental XRD data for the tetragonal phase<sup>30</sup> is displayed in Fig. 4b for comparison against our predictions. The phase was refined as  $I4_1/acd$  which, to the best of our knowledge, has not been previously reported for an  $\text{ABX}_3$  perovskite. We find good

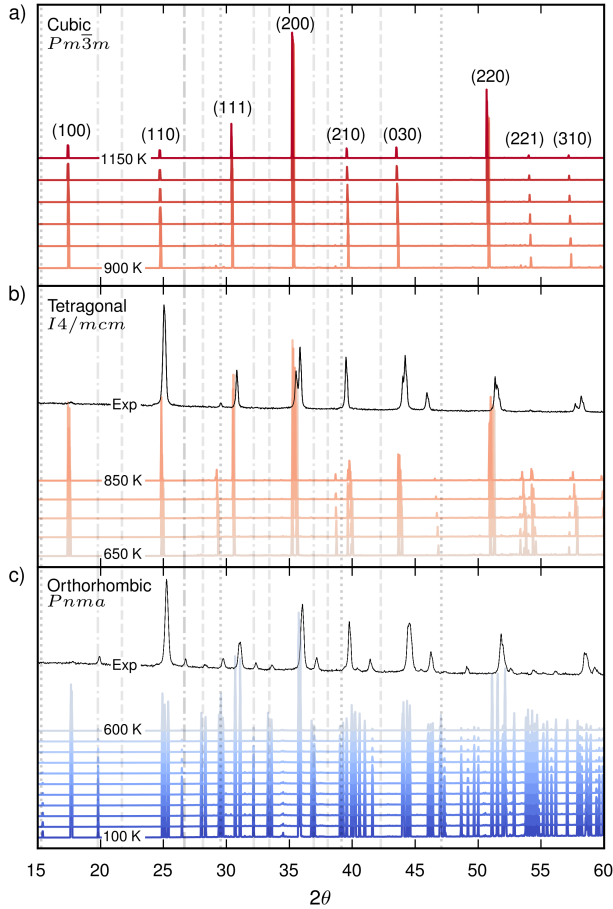


Figure 4: Static structure factor evaluated for three perovskite phases from 100 K to 1150 K in intervals of 50 K. A Cu  $K\alpha$  value of 1.5406 Å was used for the  $q$  to  $\theta$  conversion. Cubic  $Pm\bar{3}m$  peaks are indexed. Superlattice peaks (up to the third Brillouin Zone) associated with R-, M- and X-point distortions are indexed and marked with dotted, dashed and dash-dotted lines, respectively. Superlattice peaks across all BZ are displayed in the Supplementary Information. Experimental XRD data of the orthorhombic (303 K) and tetragonal (923 K) phases from Ref. 30 are plotted in black.

agreement with our predicted static structure factors for the higher-symmetry  $I4/mcm$  phase: two R-mode reflections are identified in the experimental data at  $2\theta$  values  $29^\circ$  and  $47^\circ$ , with the third possibly forming a shoulder at  $39^\circ$ .

Below 600 K, an abrupt change is observed due to the first-order phase transition into the orthorhombic phase (Fig. 4c). M-point and R-point distortions result in the appearance of additional superlattice peaks, alongside further peak splitting. Superlattice peaks associated with a X-mode distortion also appear at  $20^\circ$ ,  $26^\circ$ ,  $32^\circ$  and  $37^\circ$ . This is likely associated with the cation off-centering frequently observed when R-point and M-point distortions operate in tandem.<sup>62</sup> These effects are also identified in experimental XRD data measured at  $300^\circ$ .<sup>30</sup>

## 4 Conclusions

Chalcogenide perovskites, in particular  $BaZrS_3$ , show great potential for applications in optoelectronic and thermoelectric technologies. However several aspects of fundamental material behavior, including polymorphic phase transitions, have not yet been explored in detail. In addition, experimental characterisations of the structure through Raman spectroscopy and X-ray diffraction give conflicting results. We address this problem by developing a machine learning potential for  $BaZrS_3$  trained on hybrid DFT calculations. This is used to drive MD simulations to predict the lattice dynamics and phase equilibrium across a wide range of temperatures and pressures.

The structural and thermodynamic properties derived from heating simulations reveal a series of transitions from orthorhombic  $Pnma$ -to-tetragonal  $I4/mcm$ -to-cubic  $Pm\bar{3}m$  with increasing temperature. Whilst this sequence of structures—from the low-symmetry  $Pnma$  phase to the high-symmetry  $Pm\bar{3}m$  phase—is commonly observed in perovskite materials, to the best of our knowledge this is the first report for  $BaZrS_3$ . There is no evidence for additional transitions beyond these before melting. The predicted character of each transition—

first-order  $Pnma$ -to- $I4/mcm$  and second-order  $I4/mcm$ -to- $Pm\bar{3}m$ —is in agreement with those allowed by group-subgroup relationships.

Both phase transitions occur above 600 K, which agrees with experimental characterisation showing  $BaZrS_3$  forms in the orthorhombic  $Pnma$  phase at ambient temperature and pressure. In addition, the temperature-dependent structure factors align well with published X-ray diffraction data, supporting our prediction of an orthorhombic-to-tetragonal phase transition and validating our overall approach. Tracking the heat capacity across the relevant temperature range, e.g., through differential scanning calorimetry, is likely to provide useful insight into this first-order transition. The second-order transition at 880 K is more difficult to characterise due to the concurrent high-temperature oxidation processes; further spectroscopic or diffraction studies in an inert atmosphere may be required for experimental confirmation.

## 5 Data Availability Statement

The NEP models generated in this study are openly available via Zenodo at [doi.org/xyz](https://doi.org/xyz). The raw data from the DFT calculations have been uploaded to the NOMAD repository [doi.org/xyz](https://doi.org/xyz).

## Acknowledgements

P.K. is grateful for funding through the Turing Scheme, which facilitated a research visit to Chalmers University of Technology. P.K. also acknowledges support from the UK Engineering and Physical Sciences Research Council (EPSRC) CDT in the Renewable Energy Northeast Universities (ReNU) for funding through EPSRC Grant EP/S023836/1. This work used the Oswald High-Performance Computing Facility operated by Northumbria University (UK). Via our membership in the UK's HEC Materials Chemistry Consortium, which is funded by EPSRC (EP/X035859), this work used the

ARCHER2 UK National Supercomputing Service. We are grateful to the UK Materials and Molecular Modelling Hub for computational resources, which is partially funded by EPSRC (EP/T022213/1, EP/W032260/1, and EP/P020194/1).

This work has also been supported by the Swedish Research Council (Nos. 2020-04935 and 2021-05072), and the Chalmers Initiative for Advancement of Neutron and Synchrotron Techniques. Some of the computations were enabled by resources provided by the National Academic Infrastructure for Supercomputing in Sweden (NAISS) at C3SE, partially funded by the Swedish Research Council through grant agreement no. 2022-06725.

## References

- (1) Sun, Y.-Y.; Agiorgousis, M. L.; Zhang, P.; Zhang, S. Chalcogenide perovskites for photovoltaics. *Nano letters* **2015**, *15*, 581–585.
- (2) Sopiha, K. V.; Comparotto, C.; Márquez, J. A.; Scragg, J. J. Chalcogenide perovskites: tantalizing prospects, challenging materials. *Adv. Opt. Mater.* **2022**, *10*, 2101704.
- (3) Tiwari, D.; Hutter, O. S.; Longo, G. Chalcogenide perovskites for photovoltaics: current status and prospects. *J. Phys.: Energy* **2021**, *3*, 034010.
- (4) Jaramillo, R.; Ravichandran, J. In praise and in search of highly-polarizable semiconductors: Technological promise and discovery strategies. *APL Mater.* **2019**, *7*, 100902.
- (5) Choi, J. W.; Shin, B.; Gorai, P.; Hoyer, R. L.; Palgrave, R. Emerging earth-abundant solar absorbers. 2022.
- (6) Nishigaki, Y.; Nagai, T.; Nishiwaki, M.; Aizawa, T.; Kozawa, M.; Hanzawa, K.; Kato, Y.; Sai, H.; Hiramatsu, H.; Hosono, H.; others Extraordinary strong

- band-edge absorption in distorted chalcogenide perovskites. *Solar Rrl* **2020**, *4*, 1900555.
- (7) Ravi, V. K.; Yu, S. H.; Rajput, P. K.; Nayak, C.; Bhattacharyya, D.; Chung, D. S.; Nag, A. Colloidal BaZrS<sub>3</sub> chalcogenide perovskite nanocrystals for thin film device fabrication. *Nanoscale* **2021**, *13*, 1616–1623.
- (8) Wu, X.; Gao, W.; Chai, J.; Ming, C.; Chen, M.; Zeng, H.; Zhang, P.; Zhang, S.; Sun, Y.-Y. Defect tolerance in chalcogenide perovskite photovoltaic material BaZrS<sub>3</sub>. *Science China Materials* **2021**, *64*, 2976–2986.
- (9) Yuan, Z.; Dahliah, D.; Claes, R.; Pike, A.; Fenning, D. P.; Rignanese, G.-M.; Hautier, G. Assessing carrier mobility, dopability, and defect tolerance in the chalcogenide perovskite BaZrS<sub>3</sub>. *arXiv preprint arXiv:2405.09793* **2024**,
- (10) Yu, Z.; Wei, X.; Zheng, Y.; Hui, H.; Bian, M.; Dhole, S.; Seo, J.-H.; Sun, Y.-Y.; Jia, Q.; Zhang, S.; others Chalcogenide perovskite BaZrS<sub>3</sub> thin-film electronic and optoelectronic devices by low temperature processing. *Nano Energy* **2021**, *85*, 105959.
- (11) Yang, R.; Jess, A. D.; Fai, C.; Hages, C. J. Low-temperature, solution-based synthesis of luminescent chalcogenide perovskite BaZrS<sub>3</sub> nanoparticles. *Journal of the American Chemical Society* **2022**, *144*, 15928–15931.
- (12) Pradhan, A. A.; Uible, M. C.; Agarwal, S.; Turnley, J. W.; Khandelwal, S.; Peterson, J. M.; Blach, D. D.; Swope, R. N.; Huang, L.; Bart, S. C.; others Synthesis of BaZrS<sub>3</sub> and BaHfS<sub>3</sub> chalcogenide perovskite films using single-phase molecular precursors at moderate temperatures. *Angewandte Chemie* **2023**, *135*, e202301049.
- (13) Comparotto, C.; Strom, P.; Donzel-Gargand, O.; Kubart, T.; Scragg, J. J. Synthesis of BaZrS<sub>3</sub> perovskite thin films at a moderate temperature on conductive substrates. *ACS Applied Energy Materials* **2022**, *5*, 6335–6343.
- (14) Turnley, J. W.; Vincent, K. C.; Pradhan, A. A.; Panicker, I.; Swope, R.; Uible, M. C.; Bart, S. C.; Agrawal, R. Solution deposition for chalcogenide perovskites: a low-temperature route to BaMS<sub>3</sub> materials (M= Ti, Zr, Hf). *Journal of the American Chemical Society* **2022**, *144*, 18234–18239.
- (15) Sharma, S.; Ward, Z.; Bhimani, K.; Li, K.; Lakhnot, A.; Jain, R.; Shi, S.-F.; Terrones, H.; Koratkar, N. Bandgap tuning in BaZrS<sub>3</sub> perovskite thin films. *ACS Applied Electronic Materials* **2021**, *3*, 3306–3312.
- (16) Sadeghi, I.; Van Sambeek, J.; Simonian, T.; Xu, M.; Ye, K.; Cai, T.; Nicolosi, V.; LeBeau, J. M.; Jaramillo, R. Expanding the perovskite periodic table to include chalcogenide alloys with tunable band gap spanning 1.5–1.9 eV. *Advanced Functional Materials* **2023**, *33*, 2304575.
- (17) Meng, W.; Saparov, B.; Hong, F.; Wang, J.; Mitzi, D. B.; Yan, Y. Alloying and defect control within chalcogenide perovskites for optimized photovoltaic application. *Chemistry of Materials* **2016**, *28*, 821–829.
- (18) Dallas, P.; Gkini, K.; Kaltzoglou, A.; Givalou, L.; Konstantakou, M.; Orfanoudakis, S.; Boukos, N.; Sakellis, E.; Tsipas, P.; Kalafatis, A.; others Exploring the potential of powder-to-film processing for proof-of-concept BaZrS<sub>3</sub> perovskite solar cells. *Materials Today Communications* **2024**, *39*, 108608.
- (19) Osei-Agyemang, E.; Koratkar, N.; Balasubramanian, G. Examining the electron transport in chalcogenide perovskite BaZrS<sub>3</sub>. *Journal of Materials Chemistry C* **2021**, *9*, 3892–3900.

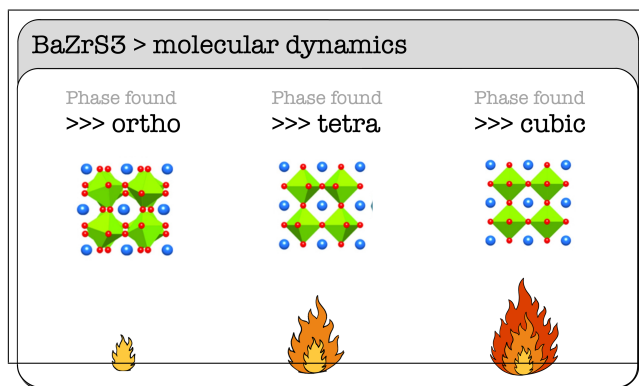


- (20) Osei-Agyemang, E.; Balasubramanian, G. Understanding the extremely poor lattice thermal transport in chalcogenide perovskite BaZrS<sub>3</sub>. *ACS Applied Energy Materials* **2019**, *3*, 1139–1144.
- (21) Yang, Z.; Han, Y.; Liang, Y.; Shen, W.; Zhang, Z.; Fang, C.; Wang, Q.; Wan, B.; Chen, L.; Zhang, Y.; others Chalcogenide perovskite BaZrS<sub>3</sub> bulks for thermoelectric conversion with ultra-high carrier mobility and low thermal conductivity. *Acta Materialia* **2024**, 120156.
- (22) Jaykhedkar, N.; Bystrický, R.; Sýkora, M.; Bučko, T. How the temperature and composition govern the structure and band gap of Zr-based chalcogenide perovskites: Insights from ML accelerated AIMD. *Inorganic Chemistry* **2023**, *62*, 12480–12492.
- (23) Comparotto, C.; Davydova, A.; Ericson, T.; Riekehr, L.; Moro, M. V.; Kubart, T.; Scragg, J. Chalcogenide perovskite BaZrS<sub>3</sub>: thin film growth by sputtering and rapid thermal processing. *ACS Applied Energy Materials* **2020**, *3*, 2762–2770.
- (24) Xu, J.; Fan, Y.; Tian, W.; Ye, L.; Zhang, Y.; Tian, Y.; Han, Y.; Shi, Z. Enhancing the optical absorption of chalcogenide perovskite BaZrS<sub>3</sub> by optimizing the synthesis and post-processing conditions. *Journal of Solid State Chemistry* **2022**, *307*, 122872.
- (25) Niu, S.; Zhao, B.; Ye, K.; Bianco, E.; Zhou, J.; McConney, M. E.; Settens, C.; Haiges, R.; Jaramillo, R.; Ravichandran, J. Crystal growth and structural analysis of perovskite chalcogenide BaZrS<sub>3</sub> and Ruddlesden–Popper phase Ba<sub>3</sub>Zr<sub>2</sub>S<sub>7</sub>. *Journal of Materials Research* **2019**, *34*, 3819–3826.
- (26) Mukherjee, S.; Riva, S.; Comparotto, C.; Johansson, F. O.; Man, G. J.; Phuyal, D.; Simonov, K. A.; Just, J.; Klementiev, K.; Butorin, S. M.; others Interplay between growth mechanism, materials chemistry, and band gap characteristics in sputtered thin films of chalcogenide perovskite BaZrS<sub>3</sub>. *ACS Applied Energy Materials* **2023**, *6*, 11642–11653.
- (27) Gross, N.; Sun, Y.-Y.; Perera, S.; Hui, H.; Wei, X.; Zhang, S.; Zeng, H.; Weinstein, B. Stability and band-gap tuning of the chalcogenide perovskite BaZrS<sub>3</sub> in Raman and optical investigations at high pressures. *Physical Review Applied* **2017**, *8*, 044014.
- (28) Filippone, S.; Zhao, B.; Niu, S.; Koocher, N. Z.; Silevitch, D.; Fina, I.; Rondinelli, J. M.; Ravichandran, J.; Jaramillo, R. Discovery of highly polarizable semiconductors BaZrS<sub>3</sub> and Ba<sub>3</sub>Zr<sub>2</sub>S<sub>7</sub>. *Physical Review Materials* **2020**, *4*, 091601.
- (29) Kayastha, P.; Tiwari, D.; Holland, A.; Hutter, O. S.; Durose, K.; Whalley, L. D.; Longo, G. High-Temperature Equilibrium of 3D and 2D Chalcogenide Perovskites. *Solar RRL* **2023**, *7*, 2201078.
- (30) Bystrický, R.; Tiwari, S. K.; Hutár, P.; Sýkora, M. Thermal Stability of Chalcogenide Perovskites. *Inorganic Chemistry* **2024**, *63*, 12826–12838.
- (31) Ye, K.; Menahem, M.; Salzillo, T.; Knoop, F.; Zhao, B.; Niu, S.; Hellman, O.; Ravichandran, J.; Jaramillo, R.; Yaffe, O. Differing vibrational properties of halide and chalcogenide perovskite semiconductors and impact on optoelectronic performance. *Physical Review Materials* **2024**, *8*, 085402.
- (32) Redfern, S. A. High-temperature structural phase transitions in perovskite. *Journal of Physics: Condensed Matter* **1996**, *8*, 8267.
- (33) Fransson, E.; Wiktor, J.; Erhart, P. Phase transitions in inorganic halide perovskites from machine-learned potentials. *The Journal of Physical Chemistry C* **2023**, *127*, 13773–13781.

- (34) Fransson, E.; Rahm, J. M.; Wiktor, J.; Erhart, P. Revealing the Free Energy Landscape of Halide Perovskites: Metastability and Transition Characters in CsPbBr<sub>3</sub> and MAPbI<sub>3</sub>. *Chemistry of Materials* **2023**, *35*, 8229–8238.
- (35) Zulkepli, N.; Yunas, J.; Mohamed, M. A.; Hamzah, A. A. Review of thermoelectric generators at low operating temperatures: working principles and materials. *Micro-machines* **2021**, *12*, 734.
- (36) Fan, Z. et al. GPUMD: A package for constructing accurate machine-learned potentials and performing highly efficient atomistic simulations. *The Journal of Chemical Physics* **2022**, *157*, 114801.
- (37) Larsen, A. H. et al. The atomic simulation environment—a Python library for working with atoms. *Journal of Physics: Condensed Matter* **2017**, *29*, 273002.
- (38) Lindgren, E.; Rahm, M.; Fransson, E.; Eriksson, F.; Österbacka, N.; Fan, Z.; Erhart, P. calorine: A Python package for constructing and sampling neuroevolution potential models. *Journal of Open Source Software* **2024**, *9*, 6264.
- (39) Glazer, A. M. The classification of tilted octahedra in perovskites. *Acta Crystallographica Section B: Structural Crystallography and Crystal Chemistry* **1972**, *28*, 3384–3392.
- (40) Howard, C. J.; Stokes, H. T. Group-theoretical analysis of octahedral tilting in perovskites. *Acta Crystallographica Section B: Structural Science* **1998**, *54*, 782–789.
- (41) Blum, V.; Gehrke, R.; Hanke, F.; Havu, P.; Havu, V.; Ren, X.; Reuter, K.; Scheffler, M. Ab initio molecular simulations with numeric atom-centered orbitals. *Computer Physics Communications* **2009**, *180*, 2175–2196.
- (42) Krukau, A. V.; Vydrov, O. A.; Izmaylov, A. F.; Scuseria, G. E. Influence of the exchange screening parameter on the performance of screened hybrid functionals. *J. Chem. Phys.* **2006**, *125*, 224106.
- (43) Togo, A. First-principles phonon calculations with phonopy and phono3py. *Journal of the Physical Society of Japan* **2023**, *92*, 012001.
- (44) Fransson, E.; Rosander, P.; Eriksson, F.; Rahm, J. M.; Tadano, T.; Erhart, P. Limits of the phonon quasi-particle picture at the cubic-to-tetragonal phase transition in halide perovskites. *Communications Physics* **2023**, *6*, 173.
- (45) Frenkel, D.; Ladd, A. J. C. New Monte Carlo Method to Compute the Free Energy of Arbitrary Solids. Application to the Fcc and Hcp Phases of Hard Spheres. *The Journal of Chemical Physics* **1984**, *81*, 3188–3193.
- (46) Fransson, E.; Slabanja, M.; Erhart, P.; Wahnström, G. dynasor —A Tool for Extracting Dynamical Structure Factors and Current Correlation Functions from Molecular Dynamics Simulations. *Advanced Theory and Simulations* **2021**, *4*, 2000240.
- (47) Tilley, R. J. *Perovskites: structure-property relationships*; John Wiley & Sons, 2016.
- (48) Lufaso, M. W.; Woodward, P. M. Jahn–Teller distortions, cation ordering and octahedral tilting in perovskites. *Acta Crystallographica Section B: Structural Science* **2004**, *60*, 10–20.
- (49) Howard, C. J.; Stokes, H. T. Structures and phase transitions in perovskites—a group-theoretical approach. *Acta Crystallographica Section A: Foundations of Crystallography* **2005**, *61*, 93–111.
- (50) Pallikara, I.; Kayastha, P.; Skelton, J. M.; Whalley, L. D. The physical significance of imaginary phonon modes in crystals. *Electronic Structure* **2022**, *4*, 033002.

- (51) Lelieveld, R.; Ijdo, D. Sulphides with the GdFeO<sub>3</sub> structure. *Acta Crystallographica Section B: Structural Crystallography and Crystal Chemistry* **1980**, *36*, 2223–2226.
- (52) Okai, B.; Takahashi, K.; Saeki, M.; Yoshimoto, J. Preparation and crystal structures of some complex sulphides at high pressures. *Materials research bulletin* **1988**, *23*, 1575–1584.
- (53) Perera, S.; Hui, H.; Zhao, C.; Xue, H.; Sun, F.; Deng, C.; Gross, N.; Milleville, C.; Xu, X.; Watson, D. F.; others Chalcogenide perovskites—an emerging class of ionic semiconductors. *Nano Energy* **2016**, *22*, 129–135.
- (54) Landau, L. D.; Lifshitz, E. M. *Statistical Physics: Volume 5*; Elsevier, 2013; Vol. 5.
- (55) Stokes, H. T.; Hatch, D. M. Group-subgroup structural phase transitions: A comparison with existing tables. *Physical Review B* **1984**, *30*, 4962.
- (56) Niu, S.; Milam-Guerrero, J.; Zhou, Y.; Ye, K.; Zhao, B.; Melot, B. C.; Ravichandran, J. Thermal stability study of transition metal perovskite sulfides. *Journal of Materials Research* **2018**, *33*, 4135–4143.
- (57) Choi, M.-J.; Lee, J.-W.; Jang, H. W. Strain Engineering in Perovskites: Mutual Insight on Oxides and Halides. *Advanced Materials* **2024**, *36*, 2308827.
- (58) Angel, R. J.; Zhao, J.; Ross, N. L. General rules for predicting phase transitions in perovskites due to octahedral tilting. *Physical review letters* **2005**, *95*, 025503.
- (59) Cohen, A.; Brenner, T. M.; Klarbring, J.; Sharma, R.; Fabini, D. H.; Korobko, R.; Nayak, P. K.; Hellman, O.; Yaffe, O. Diverging Expressions of Anharmonicity in Halide Perovskites. *Advanced Materials* **2022**, *34*, 2107932.
- (60) Menahem, M.; Benshalom, N.; Asher, M.; Aharon, S.; Korobko, R.; Hellman, O.; Yaffe, O. Disorder origin of Raman scattering in perovskite single crystals. *Physical Review Materials* **2023**, *7*, 044602.
- (61) Rosander, P.; Fransson, E.; Österbacka, N.; Erhart, P.; Wahnström, G. Untangling the Raman spectrum of cubic and tetragonal BaZrO<sub>3</sub>. *arXiv preprint arXiv:2409.16161* **2024**,
- (62) Glazer, A. M. Simple ways of determining perovskite structures. *Acta Crystallographica Section A* **1975**, *31*, 756–762.

# TOC Graphic



**Supporting Information:****Octahedral tilt-driven phase transitions in BaZrS<sub>3</sub> chalcogenide perovskite**Prakriti Kayastha<sup>1</sup>, Erik Fransson<sup>2</sup>, Paul Erhart<sup>2</sup>, and Lucy Whalley<sup>1</sup><sup>1</sup> *Department of Physics, Chalmers University of Technology, SE-41296, Gothenburg, Sweden*<sup>2</sup> *Department of Mathematics, Physics and Electrical Engineering, Northumbria University, Newcastle upon Tyne, NE1 8QH, United Kingdom*

November 22, 2024

**Contents**

<b>Methods</b>	<b>2</b>
Density Functional Theory calculations . . . . .	2
Molecular Dynamics . . . . .	2
<b>NEP model validation</b>	<b>4</b>
Comparison of phonon dispersion predicted from DFT and NEP . . . . .	5
<b>Mode projections for Glazer tilt structures</b>	<b>6</b>
<b>Recovery of the orthorhombic phase during cooling at 1 GPa</b>	<b>7</b>
<b>Finite-temperature phonons from molecular dynamics</b>	<b>8</b>
<b>Phase transition temperature using the harmonic approximation</b>	<b>9</b>
<b>Perovskite bond compressibility</b>	<b>10</b>
<b>Static structure factor</b>	<b>11</b>
<b>Supplemental References</b>	<b>12</b>

# Methods

We constructed neuroevolution potential (NEP) models by employing the iterative strategy outlined in Ref. ? . The GPUMD package in version 3.9.4<sup>36?</sup> ? was used to build the NEP model and run the molecular dynamics (MD) simulations. The ASE<sup>37</sup> and CALORINE<sup>38</sup> packages were used to prepare the training structures, set up MD simulations and post-process the results.

The initial training set contained strained primitive structures and rattled supercells of the cubic ( $Pm\bar{3}m$ ), tetragonal ( $I4/mcm$ ) and orthorhombic ( $Pnma$ ) perovskite phases. Random displacements were generated using the HIPHIVE package<sup>?</sup> . Additionally, we included structures corresponding to each of the 15 unique perovskite tilt patterns as specified by Glazer.<sup>39</sup>

The initial model was trained using density functional theory (DFT) data generated with the PBEsol exchange-correlation functional<sup>?</sup> . For each structure in the training set, we calculated the formation energy (relative to the elemental phases), stress tensor and forces. This model was then used to run MD simulations in the NPT ensemble, over a temperature and pressure range of 0 K to 1200 K and  $-5$  GPa to 20 GPa respectively, with varying supercell sizes, containing between 20 and 500 atoms. Snapshots from the MD simulations were randomly selected and added to the training set, after which the model was retrained.

Finally, a higher accuracy training set was generated using DFT with the hybrid functional HSE06<sup>42</sup>. Here we carried out single-point calculations on all 1187 training structures generated during the construction of the PBEsol-based model. Stress tensors for structures containing more than 60 atoms were not evaluated as the memory requirements for these calculations were prohibitively large. A comparison of models at the PBEsol level of theory shows that using a sub-set of stress tensors does not impact the predicted phase transition temperature or other properties of interest.

## Density Functional Theory calculations

The training data for each NEP model was generated using DFT calculations to evaluate the formation energies (relative to elemental phases), stress tensors and forces. These calculations were performed using the all-electron numeric atom-centered orbital code FHI-aims<sup>41</sup>. FHI-vibes<sup>?</sup> was used for pre and post-processing of DFT data. All DFT calculations used the *light* basis set and a Monkhorst-Pack  $k$ -point mesh with a minimum  $k$ -spacing of  $0.2/\text{\AA}$ . For single-point calculations, the charge density was converged to an accuracy of  $10^{-6}$ , forces to  $10^{-5}$  eV/ $\text{\AA}$  and stresses to  $10^{-4}$  eV/ $\text{\AA}^3$ . Geometry relaxations were carried out using the symmetry-constrained relaxation scheme as implemented in ASE<sup>37</sup>, until the maximal force component was below  $10^{-3}$  eV/ $\text{\AA}$ .

Harmonic phonon dispersions at 0 K were evaluated using the PHONOPY package<sup>43</sup> with a  $2 \times 2 \times 2$  supercell and a  $0.01 \text{\AA}$  displacement distance.

## Molecular Dynamics

MD simulations were carried out using the GPUMD software<sup>?</sup> with a timestep of 1 fs. The ASE<sup>37</sup> and calorine<sup>38</sup> packages were used to set up the MD simulations and post-process the results. Heating and cooling simulations were run in the NPT ensemble between 0 K to 1200 K for 200 ns using a supercell consisting of about 40 960 atoms. The potential energy and lattice parameters were recorded every 100 fs to discern phase transitions.

Free energy calculations were carried out via thermodynamic integration (TI) using an Einstein crystal as reference Hamiltonian (also referred to as the Frenkel-Ladd method<sup>45</sup>) as outlined in Ref. ? . The free energy of the system described by the NEP,  $F_{\text{NEP}}$ , is obtained from

$$F_{\text{NEP}} - F_{\text{Ein}} = \int_0^1 \left\langle \frac{dH(\lambda)}{d\lambda} \right\rangle_H d\lambda, \tag{S1}$$

where the integration is carried out over the Kirkwood coupling parameter  $\lambda$ <sup>?</sup>,  $F_{\text{Ein}}$  is the analytically known classical free energy of an Einstein crystal, and the Hamiltonian is  $H(\lambda) = (1 - \lambda) H_{\text{Ein}} + \lambda H_{\text{NEP}}$ , as implemented in GPUMD. Here, the ensemble average  $\langle \dots \rangle_H$  is sampled using the Hamiltonian  $H(\lambda)$ . The Gibbs free energy can then be obtained by  $G = F + PV$ . TI simulations were

run for 0.05 ns using a spring constant of  $4 \text{ eV}/\text{\AA}^2$  using a supercell consisting of 23 040 atoms. These simulations were run in the NVT ensemble with lattice parameters obtained from NPT simulations.

The static structure factor,  $S(\mathbf{q})$ , is calculated from NVT simulations using the DYNASOR package<sup>46</sup> as

$$S(\mathbf{q}) = \frac{1}{N} \left\langle \sum_i^N \sum_j^N \exp [i\mathbf{q} \cdot (\mathbf{r}_i(t) - \mathbf{r}_j(t))] \right\rangle, \quad (\text{S2})$$

where  $\mathbf{r}_i(t)$  is the position of atom  $i$  at time  $t$  and the sums run over all atoms.

We employ phonon mode projection to analyze and classify both relaxed structures and snapshots from MD simulations as done in<sup>44</sup>. The atomic displacements  $\mathbf{u}$  can be projected on a mode  $\lambda$ , with the supercell eigenvector  $\mathbf{e}_\lambda$ , via

$$Q_\lambda = \mathbf{u} \cdot \mathbf{e}_\lambda$$

Here, the phonon supercell eigenvector of the  $R$  and  $M$  tilt modes are obtained with PHONOPY<sup>7</sup>, and symmetrized such that each of the three degenerate modes corresponds to tilting around the x, y and z direction respectively.

# NEP model validation

Our final training set consists of 1187 structures. Energies, forces, and stress tensors are evaluated using the HSE06 functional. Energies and forces are evaluated for all structures. However, due to large memory requirements, to evaluate stress tensors are only evaluated for structures with less than 60 atoms in the unit cell. Energy and force errors are reported for the entire training set of 1187 structures. Virial and stress errors are only reported for structures where the DFT stress tensors were evaluated.

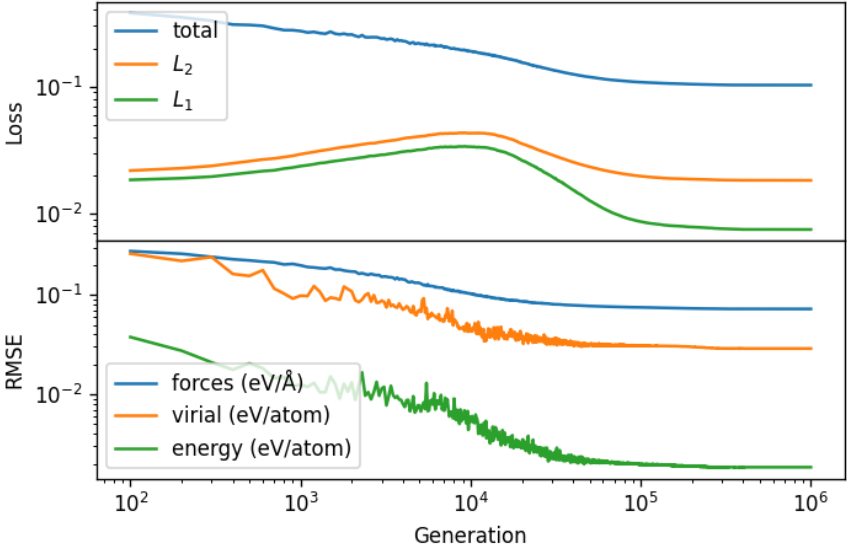


Figure S1: Loss curves for the HSE06 model

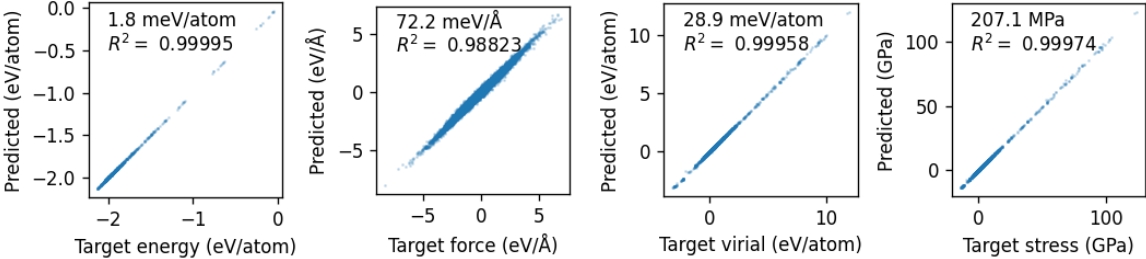


Figure S2: Parity plot for the HSE06 model. In structures for which the stress tensors have not been evaluated, large values predicted by NEP are ignored.



## Comparison of phonon dispersion predicted from DFT and NEP

The 0 K harmonic phonon spectra for  $\text{BaZrS}_3$  in its three observed phases are displayed. The dashed black line corresponds to that generated with our NEP model, the solid blue is calculated using DFT-calculated forces. The largest discrepancies correspond to high-frequency modes strongly associated with the sulfur species. <sup>?</sup>

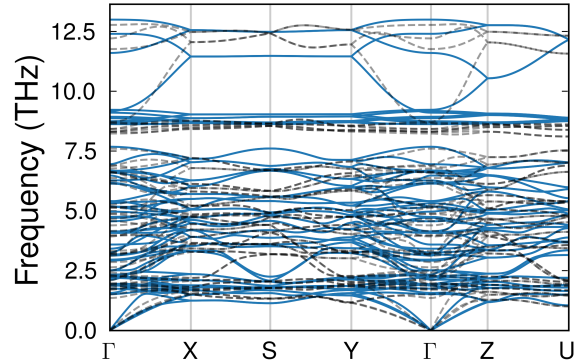


Figure S3: Pnma DFT (solid blue) vs NEP (dashed black) phonons

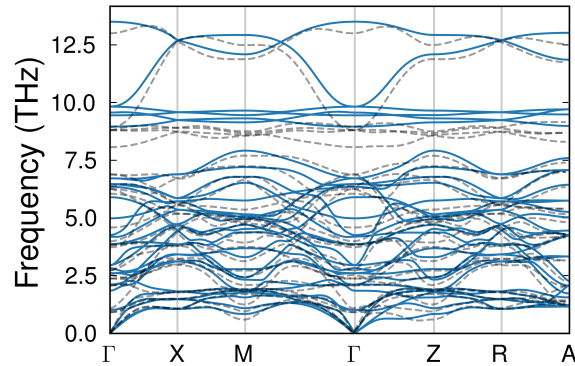


Figure S4: I4/mcm DFT (solid blue) vs NEP (dashed black) phonons

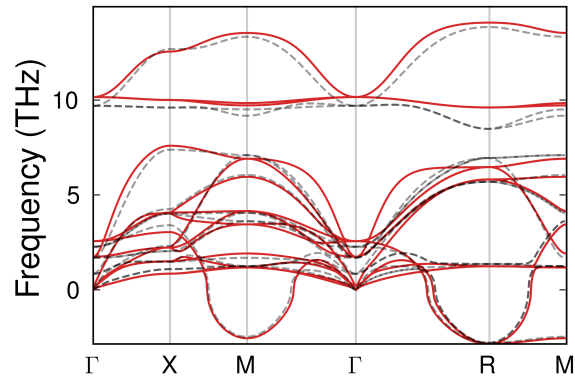


Figure S5: Pm-3m DFT (solid red) vs NEP (dashed black) phonons

# Mode projections for Glazer tilt structures

In our comprehensive evaluation of all 15 Glazer-tilted structures we observe that  $I4/mcm$  and its subgroups ( $P4_2/nmc$ ,  $Cmcm$ ,  $C2/m$ ,  $C2/c$ ,  $P\bar{1}$ ) have similar energies according to DFT calculations and the NEP model. Our workflow for constructing these structures was to constrain the spacegroup symmetry using the ASE<sup>37</sup> FIXSYMMETRY function. Subgroup structures which are unstable at 0 K relax to their supergroup phase with a small (but non-zero) phonon mode amplitude. The corresponding distortion lies within the tolerance factor of the symmetry-constrained relaxation ( $10^{-5}$  Å). This small difference in structure results in energies that are similar but not exactly the same. For example, the  $Cmcm$   $a^0b^+c^-$  structure relaxes to an  $I4/mcm$   $a^0b^0c^-$  equivalent structure with a small mode projection value for the  $b^+$  tilt. This results in a small energy difference (0.2 meV) between the two phases.

Similar observations can be made for the  $P2_1/m$  and  $Pnma$  phases, and the  $Immm$  and  $P4/mbm$  phases.

Space group	$M_x$	$M_y$	$M_z$	$R_x$	$R_y$	$R_z$
$Pm\bar{3}m$ (221)	0.000000	0.000000	-0.000000	-0.000000	0.000000	0.000000
$I4/mcm$ (140)	0.000000	0.000000	0.000000	0.000000	0.000000	0.575006
$P4/mbm$ (127)	0.000000	0.000000	0.548092	0.000000	0.000000	0.000000
$Imma$ (74)	0.000000	0.000000	0.000000	0.000000	0.373962	0.373962
$C2/m$ (12)	0.000000	0.000000	0.000000	0.000000	0.000030	0.575030
$Cmcm$ (63)	0.000000	0.000002	0.000000	0.000000	0.000000	0.575030
$I4/mmm$ (139)	0.000000	0.328544	0.328544	0.000000	0.000000	0.000000
$R\bar{3}c$ (167)	0.000000	0.000000	0.000000	0.292519	0.292519	0.292519
$C2/c$ (15)	0.000000	0.000000	0.000000	0.575000	0.000016	0.000016
$P\bar{1}$ (2)	0.000000	0.000000	0.000000	0.574996	0.000037	0.000017
$I4/mmm$ (139)	0.000000	0.328544	0.328544	0.000000	0.000000	0.000000
$Pnma$ (62)	0.401595	0.000000	0.000000	0.000000	0.321830	0.321830
$P2_1/m$ (11)	0.401610	0.000000	0.000000	0.000000	0.321820	0.321830
$P4_2/nmc$ (137)	0.000001	0.000001	0.000000	0.000000	0.000000	0.575031
$Im\bar{3}$ (204)	0.251797	0.251797	0.251797	0.000000	0.000000	0.000000
$Immm$ (71)	0.548063	0.000001	0.000003	0.000000	0.000000	0.000000

Table S1: Mode projection on DFT relaxed geometries

Space group	$M_x$	$M_y$	$M_z$	$R_x$	$R_y$	$R_z$
$Pm\bar{3}m$ (221)	0.000000	0.000000	0.000000	0.000000	0.000000	0.000000
$I4/mcm$ (140)	0.000000	0.000000	0.000000	0.000000	0.000000	0.579234
$P4/mbm$ (127)	0.000000	0.000000	0.542603	0.000000	0.000000	0.000000
$Imma$ (74)	0.000000	0.000000	0.000000	0.000000	0.369080	0.369080
$C2/m$ (12)	0.000000	0.000000	0.000000	0.000000	-0.000028	0.579234
$Cmcm$ (63)	0.000000	0.000000	0.000000	0.000000	0.000000	0.579234
$I4/mmm$ (139)	0.000000	0.329391	0.329391	0.000000	0.000000	0.000000
$R\bar{3}c$ (167)	0.000000	0.000000	0.000000	0.286208	0.286208	0.286208
$C2/c$ (15)	0.000000	0.000000	0.000000	0.579234	0.000025	0.000025
$P\bar{1}$ (2)	0.000000	0.000000	0.000000	0.579233	0.000045	0.000011
$I4/mmm$ (139)	0.000000	0.329391	0.329391	0.000000	0.000000	0.000000
$Pnma$ (62)	0.400823	0.000000	0.000000	0.000000	0.326056	0.326056
$P2_1/m$ (11)	0.400821	0.000000	0.000000	0.000000	0.326061	0.326054
$P4_2/nmc$ (137)	0.000000	0.000000	0.000000	0.000000	0.000000	0.579234
$Im\bar{3}$ (204)	0.251378	0.251378	0.251378	0.000000	0.000000	0.000000
$Immm$ (71)	0.542603	0.000000	0.000000	0.000000	0.000000	0.000000

Table S2: Mode projection on NEP relaxed geometries

## Recovery of the orthorhombic phase during cooling at 1 GPa

Our cooling simulations in the main text do not recover the orthorhombic Pnma phase formed at 0 K. This stems from the numerical limitations of our simulations; the short timescales considered makes a first-order transition (with associated kinetic barrier) from the tetragonal phase implausible. Here we plot the heating and cooling runs at 1 GPa, where the orthorhombic phase is recovered around 560 K. This variation in our results is due to the stochastic nature of molecular dynamics simulations.

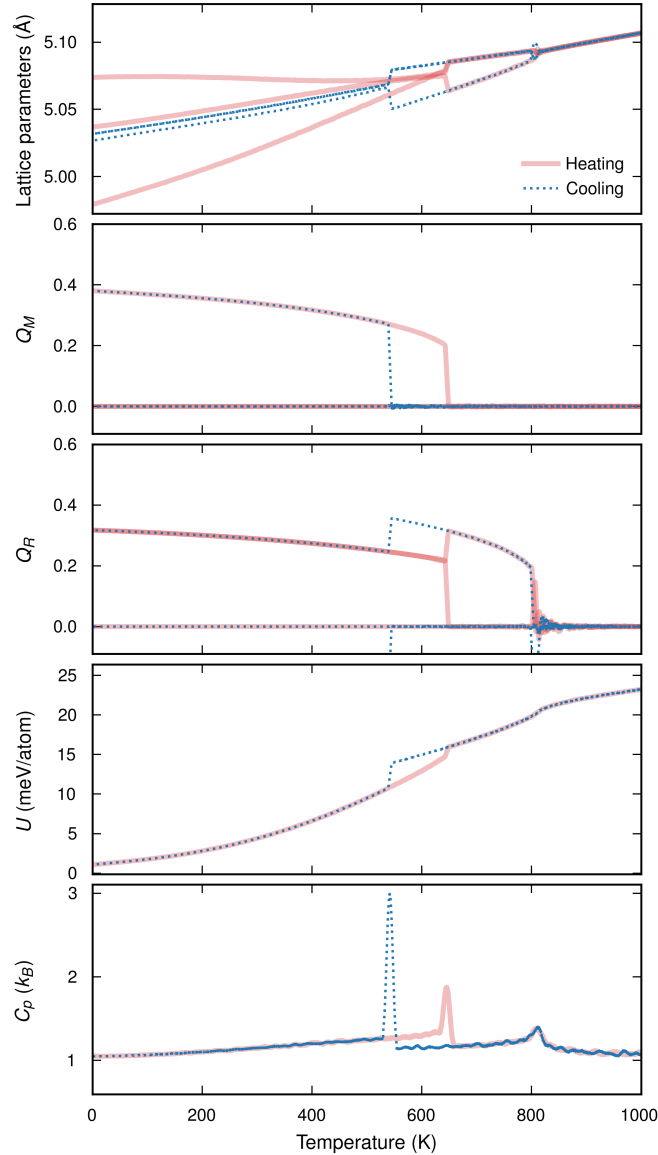


Figure S6: Heating and cooling runs at pressure 1 GPa. The orthorhombic Pnma phase is recovered in the cooling run, unlike our simulations at 0 Pa (see the main text).

## Finite-temperature phonons from molecular dynamics

The DYNASOR package<sup>46</sup> is used to calculate the spectral energy density of the  $I4/mcm$  and  $Pm\bar{3}m$  phases at various temperatures. All modes are positive across the Brillouin zone, supporting our observation of a  $I4/mcm$ -to- $Pm\bar{3}m$  transition at high temperature.

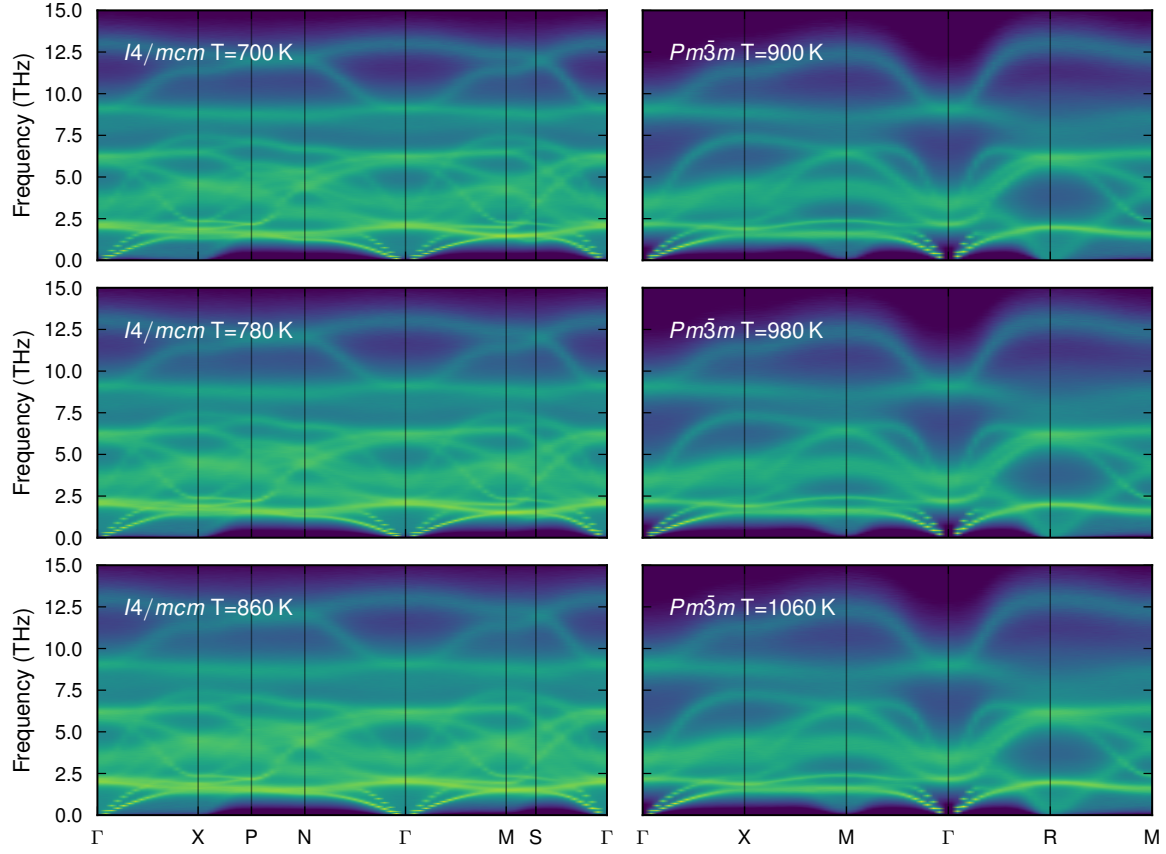


Figure S7: Spectral energy densities of the tetragonal  $I4/mcm$  and cubic  $Pm\bar{3}m$  phases of BaZrS<sub>3</sub>.

## Phase transition temperature using the harmonic approximation

Free energies of the orthorhombic ( $Pnma$ ) and tetragonal ( $I4/mcm$ ) phases are evaluated within the harmonic approximation. The phase transition temperature with DFT-calculated phonon frequencies is 460 K, with NEP-calculated frequencies it is 380 K. The phase transition temperature predicted with our fully-anharmonic molecular dynamics model (see main text) is 650 K.

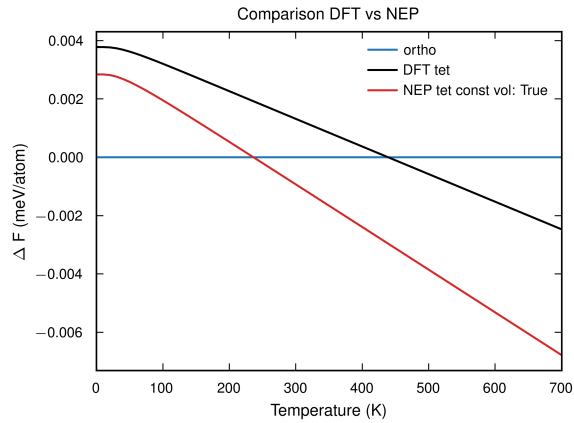


Figure S8: Free energy difference between  $Pnma$  and  $I4/mcm$  phases ( $\Delta F$ ), calculated under the harmonic approximation.

## Perovskite bond compressibility

Perovskites with lower symmetry (more tilted) structures generally exhibit a series of octahedral tilt-driven phase transitions to higher symmetry (less tilted) structures with increasing temperature. The phase transition temperature  $T_c$  can increase or decrease with pressure,  $\frac{dT_c}{dP} > 0$  or  $\frac{dT_c}{dP} < 0$  respectively.<sup>58</sup> For BaZrS<sub>3</sub> we find  $\frac{dT_c}{dP} > 0$  (Fig 3 in the main text). This behaviour can be rationalised by considering the relative compressibility of the A-X and B-X bonds.<sup>58,7</sup> If the B-X bonds forming the octahedra are relatively rigid then pressure must induce tilting to accommodate the volume reduction, resulting in the compression of the A-X bonds and a reduction in symmetry. If the A-X bonds are relatively rigid then pressure must induce a reduction in the octahedral volume through compression of the B-X bond. The ratio of the B-X and A-X bond compressibilities ( $\frac{\beta_B}{\beta_A}$ ) can be used to indicate how the phase transition temperature will vary as a function of pressure:  $\frac{dT_c}{dP} > 0$  when  $\frac{\beta_B}{\beta_A} < 1$ , and  $\frac{dT_c}{dP} < 0$  when  $\frac{\beta_B}{\beta_A} > 1$ . The parameter  $M_i = \beta_i^{-1}$  is given by:

$$M_i = \frac{R_i N_i}{B} \exp\left(\frac{R_i - R_0}{B}\right) \quad (\text{S3})$$

where  $N_i$  is the coordination number,  $R_i$  average bond distance (to X-atoms),  $B$  is a constant with value 0.37, and  $R_0$  is the bond-valence parameter.<sup>?</sup> For BaZrS<sub>3</sub> we obtain  $\frac{\beta_B}{\beta_A} = \frac{M_A}{M_B} \approx 0.45$ . This indicates that  $\frac{dT_c}{dP} > 0$ , in agreement with our predicted phase diagram.

## Static structure factor

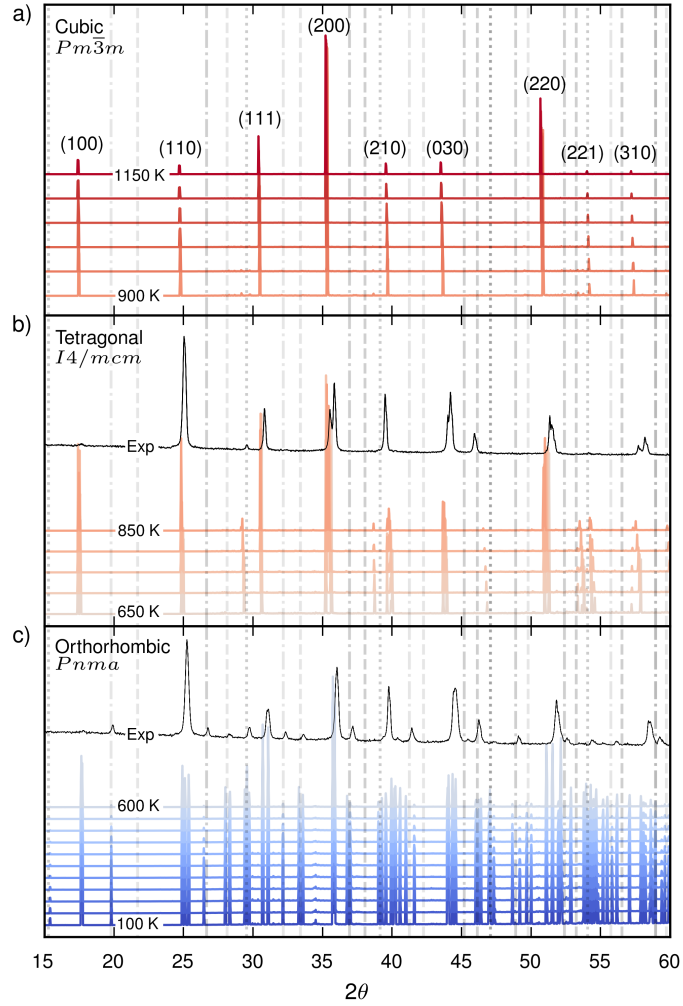


Figure S9: Static structure factor evaluated for three perovskite phases from 100 K to 1150 K in intervals of 50 K. A Cu  $K\alpha$  value of  $1.5406 \text{ \AA}$  was used for the  $q$  to  $\theta$  conversion. Cubic  $Pm\bar{3}m$  peaks are indexed. Superlattice peaks (up to the fifth Brillouin Zone) associated with R-, M- and X-point distortions are indexed and marked with dotted, dashed and dash-dotted lines, respectively. Experimental XRD data of the orthorhombic (303 K) and tetragonal (923 K) phases from Ref. 30 are plotted in black.

## Supplemental References

- [1] Sun, Y.-Y.; Agiorgousis, M. L.; Zhang, P.; Zhang, S. Chalcogenide perovskites for photovoltaics. *Nano letters* **2015**, *15*, 581–585.
- [2] Sopiha, K. V.; Comparotto, C.; Márquez, J. A.; Scragg, J. J. Chalcogenide perovskites: tantalizing prospects, challenging materials. *Adv. Opt. Mater.* **2022**, *10*, 2101704.
- [3] Tiwari, D.; Hutter, O. S.; Longo, G. Chalcogenide perovskites for photovoltaics: current status and prospects. *J. Phys.: Energy* **2021**, *3*, 034010.
- [4] Jaramillo, R.; Ravichandran, J. In praise and in search of highly-polarizable semiconductors: Technological promise and discovery strategies. *APL Mater.* **2019**, *7*, 100902.
- [5] Choi, J. W.; Shin, B.; Gorai, P.; Hoye, R. L.; Palgrave, R. Emerging earth-abundant solar absorbers. 2022.
- [6] Nishigaki, Y.; Nagai, T.; Nishiwaki, M.; Aizawa, T.; Kozawa, M.; Hanzawa, K.; Kato, Y.; Sai, H.; Hiramatsu, H.; Hosono, H.; others Extraordinary strong band-edge absorption in distorted chalcogenide perovskites. *Solar Rrl* **2020**, *4*, 1900555.
- [7] Ravi, V. K.; Yu, S. H.; Rajput, P. K.; Nayak, C.; Bhattacharyya, D.; Chung, D. S.; Nag, A. Colloidal BaZrS<sub>3</sub> chalcogenide perovskite nanocrystals for thin film device fabrication. *Nanoscale* **2021**, *13*, 1616–1623.
- [8] Wu, X.; Gao, W.; Chai, J.; Ming, C.; Chen, M.; Zeng, H.; Zhang, P.; Zhang, S.; Sun, Y.-Y. Defect tolerance in chalcogenide perovskite photovoltaic material BaZrS<sub>3</sub>. *Science China Materials* **2021**, *64*, 2976–2986.
- [9] Yuan, Z.; Dahliah, D.; Claes, R.; Pike, A.; Fenning, D. P.; Rignanese, G.-M.; Hautier, G. Assessing carrier mobility, dopability, and defect tolerance in the chalcogenide perovskite BaZrS<sub>3</sub>. *arXiv preprint arXiv:2405.09793* **2024**,
- [10] Yu, Z.; Wei, X.; Zheng, Y.; Hui, H.; Bian, M.; Dhole, S.; Seo, J.-H.; Sun, Y.-Y.; Jia, Q.; Zhang, S.; others Chalcogenide perovskite BaZrS<sub>3</sub> thin-film electronic and optoelectronic devices by low temperature processing. *Nano Energy* **2021**, *85*, 105959.
- [11] Yang, R.; Jess, A. D.; Fai, C.; Hages, C. J. Low-temperature, solution-based synthesis of luminescent chalcogenide perovskite BaZrS<sub>3</sub> nanoparticles. *Journal of the American Chemical Society* **2022**, *144*, 15928–15931.
- [12] Pradhan, A. A.; Uible, M. C.; Agarwal, S.; Turnley, J. W.; Khandelwal, S.; Peterson, J. M.; Blach, D. D.; Swope, R. N.; Huang, L.; Bart, S. C.; others Synthesis of BaZrS<sub>3</sub> and BaHfS<sub>3</sub> chalcogenide perovskite films using single-phase molecular precursors at moderate temperatures. *Angewandte Chemie* **2023**, *135*, e202301049.
- [13] Comparotto, C.; Strom, P.; Donzel-Gargand, O.; Kubart, T.; Scragg, J. J. Synthesis of BaZrS<sub>3</sub> perovskite thin films at a moderate temperature on conductive substrates. *ACS Applied Energy Materials* **2022**, *5*, 6335–6343.
- [14] Turnley, J. W.; Vincent, K. C.; Pradhan, A. A.; Panicker, I.; Swope, R.; Uible, M. C.; Bart, S. C.; Agrawal, R. Solution deposition for chalcogenide perovskites: a low-temperature route to BaMS<sub>3</sub> materials (M= Ti, Zr, Hf). *Journal of the American Chemical Society* **2022**, *144*, 18234–18239.
- [15] Sharma, S.; Ward, Z.; Bhimani, K.; Li, K.; Lakhot, A.; Jain, R.; Shi, S.-F.; Terrones, H.; Koratkar, N. Bandgap tuning in BaZrS<sub>3</sub> perovskite thin films. *ACS Applied Electronic Materials* **2021**, *3*, 3306–3312.
- [16] Sadeghi, I.; Van Sambeek, J.; Simonian, T.; Xu, M.; Ye, K.; Cai, T.; Nicolosi, V.; LeBeau, J. M.; Jaramillo, R. Expanding the perovskite periodic table to include chalcogenide alloys with tunable band gap spanning 1.5–1.9 eV. *Advanced Functional Materials* **2023**, *33*, 2304575.



- [17] Meng, W.; Saparov, B.; Hong, F.; Wang, J.; Mitzi, D. B.; Yan, Y. Alloying and defect control within chalcogenide perovskites for optimized photovoltaic application. *Chemistry of Materials* **2016**, *28*, 821–829.
- [18] Dallas, P.; Gkini, K.; Kaltzoglou, A.; Givalou, L.; Konstantakou, M.; Orfanoudakis, S.; Boukos, N.; Sakellis, E.; Tsipas, P.; Kalafatis, A.; others Exploring the potential of powder-to-film processing for proof-of-concept BaZrS<sub>3</sub> perovskite solar cells. *Materials Today Communications* **2024**, *39*, 108608.
- [19] Osei-Agyemang, E.; Koratkar, N.; Balasubramanian, G. Examining the electron transport in chalcogenide perovskite BaZrS<sub>3</sub>. *Journal of Materials Chemistry C* **2021**, *9*, 3892–3900.
- [20] Osei-Agyemang, E.; Balasubramanian, G. Understanding the extremely poor lattice thermal transport in chalcogenide perovskite BaZrS<sub>3</sub>. *ACS Applied Energy Materials* **2019**, *3*, 1139–1144.
- [21] Yang, Z.; Han, Y.; Liang, Y.; Shen, W.; Zhang, Z.; Fang, C.; Wang, Q.; Wan, B.; Chen, L.; Zhang, Y.; others Chalcogenide perovskite BaZrS<sub>3</sub> bulks for thermoelectric conversion with ultra-high carrier mobility and low thermal conductivity. *Acta Materialia* **2024**, 120156.
- [22] Jaykhedkar, N.; Bystrický, R.; Sýkora, M.; Bučko, T. How the temperature and composition govern the structure and band gap of Zr-based chalcogenide perovskites: Insights from ML accelerated AIMD. *Inorganic Chemistry* **2023**, *62*, 12480–12492.
- [23] Comparotto, C.; Davydova, A.; Ericson, T.; Riekehr, L.; Moro, M. V.; Kubart, T.; Scragg, J. Chalcogenide perovskite BaZrS<sub>3</sub>: thin film growth by sputtering and rapid thermal processing. *ACS Applied Energy Materials* **2020**, *3*, 2762–2770.
- [24] Xu, J.; Fan, Y.; Tian, W.; Ye, L.; Zhang, Y.; Tian, Y.; Han, Y.; Shi, Z. Enhancing the optical absorption of chalcogenide perovskite BaZrS<sub>3</sub> by optimizing the synthesis and post-processing conditions. *Journal of Solid State Chemistry* **2022**, *307*, 122872.
- [25] Niu, S.; Zhao, B.; Ye, K.; Bianco, E.; Zhou, J.; McConney, M. E.; Settens, C.; Haiges, R.; Jaramillo, R.; Ravichandran, J. Crystal growth and structural analysis of perovskite chalcogenide BaZrS<sub>3</sub> and Ruddlesden–Popper phase Ba<sub>3</sub>Zr<sub>2</sub>S<sub>7</sub>. *Journal of Materials Research* **2019**, *34*, 3819–3826.
- [26] Mukherjee, S.; Riva, S.; Comparotto, C.; Johansson, F. O.; Man, G. J.; Phuyal, D.; Simonov, K. A.; Just, J.; Klementiev, K.; Butorin, S. M.; others Interplay between growth mechanism, materials chemistry, and band gap characteristics in sputtered thin films of chalcogenide perovskite BaZrS<sub>3</sub>. *ACS Applied Energy Materials* **2023**, *6*, 11642–11653.
- [27] Gross, N.; Sun, Y.-Y.; Perera, S.; Hui, H.; Wei, X.; Zhang, S.; Zeng, H.; Weinstein, B. Stability and band-gap tuning of the chalcogenide perovskite BaZrS<sub>3</sub> in Raman and optical investigations at high pressures. *Physical Review Applied* **2017**, *8*, 044014.
- [28] Filippone, S.; Zhao, B.; Niu, S.; Koocher, N. Z.; Silevitch, D.; Fina, I.; Rondinelli, J. M.; Ravichandran, J.; Jaramillo, R. Discovery of highly polarizable semiconductors BaZrS<sub>3</sub> and Ba<sub>3</sub>Zr<sub>2</sub>S<sub>7</sub>. *Physical Review Materials* **2020**, *4*, 091601.
- [29] Kayastha, P.; Tiwari, D.; Holland, A.; Hutter, O. S.; Durose, K.; Whalley, L. D.; Longo, G. High-Temperature Equilibrium of 3D and 2D Chalcogenide Perovskites. *Solar RRL* **2023**, *7*, 2201078.
- [30] Bystrický, R.; Tiwari, S. K.; Hutár, P.; Sýkora, M. Thermal Stability of Chalcogenide Perovskites. *Inorganic Chemistry* **2024**, *63*, 12826–12838.
- [31] Ye, K.; Menahem, M.; Salzillo, T.; Knoop, F.; Zhao, B.; Niu, S.; Hellman, O.; Ravichandran, J.; Jaramillo, R.; Yaffe, O. Differing vibrational properties of halide and chalcogenide perovskite semiconductors and impact on optoelectronic performance. *Physical Review Materials* **2024**, *8*, 085402.

- [32] Redfern, S. A. High-temperature structural phase transitions in perovskite. *Journal of Physics: Condensed Matter* **1996**, *8*, 8267.
- [33] Fransson, E.; Wiktor, J.; Erhart, P. Phase transitions in inorganic halide perovskites from machine-learned potentials. *The Journal of Physical Chemistry C* **2023**, *127*, 13773–13781.
- [34] Fransson, E.; Rahm, J. M.; Wiktor, J.; Erhart, P. Revealing the Free Energy Landscape of Halide Perovskites: Metastability and Transition Characters in CsPbBr<sub>3</sub> and MAPbI<sub>3</sub>. *Chemistry of Materials* **2023**, *35*, 8229–8238.
- [35] Zulkepli, N.; Yunas, J.; Mohamed, M. A.; Hamzah, A. A. Review of thermoelectric generators at low operating temperatures: working principles and materials. *Micromachines* **2021**, *12*, 734.
- [36] Fan, Z. et al. GPUMD: A package for constructing accurate machine-learned potentials and performing highly efficient atomistic simulations. *The Journal of Chemical Physics* **2022**, *157*, 114801.
- [37] Larsen, A. H. et al. The atomic simulation environment—a Python library for working with atoms. *Journal of Physics: Condensed Matter* **2017**, *29*, 273002.
- [38] Lindgren, E.; Rahm, M.; Fransson, E.; Eriksson, F.; Österbacka, N.; Fan, Z.; Erhart, P. calorine: A Python package for constructing and sampling neuroevolution potential models. *Journal of Open Source Software* **2024**, *9*, 6264.
- [39] Glazer, A. M. The classification of tilted octahedra in perovskites. *Acta Crystallographica Section B: Structural Crystallography and Crystal Chemistry* **1972**, *28*, 3384–3392.
- [40] Howard, C. J.; Stokes, H. T. Group-theoretical analysis of octahedral tilting in perovskites. *Acta Crystallographica Section B: Structural Science* **1998**, *54*, 782–789.
- [41] Blum, V.; Gehrke, R.; Hanke, F.; Havu, P.; Havu, V.; Ren, X.; Reuter, K.; Scheffler, M. Ab initio molecular simulations with numeric atom-centered orbitals. *Computer Physics Communications* **2009**, *180*, 2175–2196.
- [42] Krukau, A. V.; Vydrov, O. A.; Izmaylov, A. F.; Scuseria, G. E. Influence of the exchange screening parameter on the performance of screened hybrid functionals. *J. Chem. Phys.* **2006**, *125*, 224106.
- [43] Togo, A. First-principles phonon calculations with phonopy and phono3py. *Journal of the Physical Society of Japan* **2023**, *92*, 012001.
- [44] Fransson, E.; Rosander, P.; Eriksson, F.; Rahm, J. M.; Tadano, T.; Erhart, P. Limits of the phonon quasi-particle picture at the cubic-to-tetragonal phase transition in halide perovskites. *Communications Physics* **2023**, *6*, 173.
- [45] Frenkel, D.; Ladd, A. J. C. New Monte Carlo Method to Compute the Free Energy of Arbitrary Solids. Application to the Fcc and Hcp Phases of Hard Spheres. *The Journal of Chemical Physics* **1984**, *81*, 3188–3193.
- [46] Fransson, E.; Slabanja, M.; Erhart, P.; Wahnström, G. dynasor —A Tool for Extracting Dynamical Structure Factors and Current Correlation Functions from Molecular Dynamics Simulations. *Advanced Theory and Simulations* **2021**, *4*, 2000240.
- [47] Tilley, R. J. *Perovskites: structure-property relationships*; John Wiley & Sons, 2016.
- [48] Lufaso, M. W.; Woodward, P. M. Jahn–Teller distortions, cation ordering and octahedral tilting in perovskites. *Acta Crystallographica Section B: Structural Science* **2004**, *60*, 10–20.
- [49] Howard, C. J.; Stokes, H. T. Structures and phase transitions in perovskites—a group-theoretical approach. *Acta Crystallographica Section A: Foundations of Crystallography* **2005**, *61*, 93–111.
- [50] Pallikara, I.; Kayastha, P.; Skelton, J. M.; Whalley, L. D. The physical significance of imaginary phonon modes in crystals. *Electronic Structure* **2022**, *4*, 033002.

- [51] Lelieveld, R.; Ijdo, D. Sulphides with the GdFeO<sub>3</sub> structure. *Acta Crystallographica Section B: Structural Crystallography and Crystal Chemistry* **1980**, *36*, 2223–2226.
- [52] Okai, B.; Takahashi, K.; Saeki, M.; Yoshimoto, J. Preparation and crystal structures of some complex sulphides at high pressures. *Materials research bulletin* **1988**, *23*, 1575–1584.
- [53] Perera, S.; Hui, H.; Zhao, C.; Xue, H.; Sun, F.; Deng, C.; Gross, N.; Milleville, C.; Xu, X.; Watson, D. F.; others Chalcogenide perovskites—an emerging class of ionic semiconductors. *Nano Energy* **2016**, *22*, 129–135.
- [54] Landau, L. D.; Lifshitz, E. M. *Statistical Physics: Volume 5*; Elsevier, 2013; Vol. 5.
- [55] Stokes, H. T.; Hatch, D. M. Group-subgroup structural phase transitions: A comparison with existing tables. *Physical Review B* **1984**, *30*, 4962.
- [56] Niu, S.; Milam-Guerrero, J.; Zhou, Y.; Ye, K.; Zhao, B.; Melot, B. C.; Ravichandran, J. Thermal stability study of transition metal perovskite sulfides. *Journal of Materials Research* **2018**, *33*, 4135–4143.
- [57] Choi, M.-J.; Lee, J.-W.; Jang, H. W. Strain Engineering in Perovskites: Mutual Insight on Oxides and Halides. *Advanced Materials* **2024**, *36*, 2308827.
- [58] Angel, R. J.; Zhao, J.; Ross, N. L. General rules for predicting phase transitions in perovskites due to octahedral tilting. *Physical review letters* **2005**, *95*, 025503.
- [59] Cohen, A.; Brenner, T. M.; Klarbring, J.; Sharma, R.; Fabini, D. H.; Korobko, R.; Nayak, P. K.; Hellman, O.; Yaffe, O. Diverging Expressions of Anharmonicity in Halide Perovskites. *Advanced Materials* **2022**, *34*, 2107932.
- [60] Menahem, M.; Benshalom, N.; Asher, M.; Aharon, S.; Korobko, R.; Hellman, O.; Yaffe, O. Disorder origin of Raman scattering in perovskite single crystals. *Physical Review Materials* **2023**, *7*, 044602.
- [61] Rosander, P.; Fransson, E.; Österbacka, N.; Erhart, P.; Wahnström, G. Untangling the Raman spectrum of cubic and tetragonal BaZrO<sub>3</sub>. *arXiv preprint arXiv:2409.16161* **2024**,
- [62] Glazer, A. M. Simple ways of determining perovskite structures. *Acta Crystallographica Section A* **1975**, *31*, 756–762.